Supplementary Information

CAM-CM: A Signal Deconvolution Tool for In Vivo Dynamic Contrast-enhanced Imaging of Complex Tissues

Li Chen[1,*], Tsung-Han Chan[1,2,*], Peter L. Choyke[3], Elizabeth M. C. Hillman[4], Chong-Yung Chi[2], Zaver M. Bhujwalla[5], Ge Wang[6], Sean S. Wang[7], Zsolt Szabo[5], Yue Wang[1,†]

[1]Bradley Department of Electrical and Computer Engineering and [6]School of Biomedical Engineering and Sciences, Virginia Polytechnic Institute and state University, Arlington, VA 22203, USA,
[2]Department of Electrical Engineering, National Tsing Hua University, Taiwan, ROC,
[3]Molecular Imaging Program, National Cancer Institute, NIH, Bethesda, MD 20892, USA,
[4]Department of Biomedical Engineering and Radiology, Columbia University, New York, NY 10027, USA,
[5]Department of Radiology and Radiological Science, Johns Hopkins University School of Medicine, Baltimore, MD 21205, USA,
[7]Science, Mathematics, Computer Science House, Poolesville High School, Poolesville, MD 20837, USA.

[*] Contributed equally.
[†]To whom correspondence should be addressed.

Contents

S1 BACKGROUND

In vivo dynamic contrast-enhanced imaging tools provide noninvasive methods for analyzing various functional changes associated with disease initiation, progression, and responses to therapy (McDonald, *et al.*, 2003). Typical modalities include dynamic contrast-enhanced magnetic resonance imaging (DCE-MRI) (Costouros, et al., 2002), dynamic optical imaging (Hillman, et al., 2007), positron emission tomography (Zhou, et al., 1997), and spectroscopic computed tomography (Anderson, et al., 2010). These tools exploit the dynamics of contrast accumulation and washout to produce functionally relevant images of vascular perfusion and permeability, metabolism, or gene expression, and can potentially test novel hypotheses and predict drug efficacy.

However, due to spatially-mixed tissue heterogeneity, the precise imaging-based phenotyping by these tools has been hindered by its inability to accurately resolve and characterize targeted functional tissue compartments (Hillman, *et al.*, 2007). This indistinction between contributions of different tissues to the mixed tracer signals, while often conveniently overlooked, could significantly confound pharmacokinetics compartmental modeling (CM) (Zhou, et al., 1997) and affect the accuracy of genotype-phenotype association studies (Costouros, et al., 2002; Segal, et al., 2007).

We developed convex analysis of mixtures – compartment modeling (CAM-CM) signal deconvolution tool that enables geometrically-principled, unsupervised, and accurate characterization and delineation of major functional tissue structures using dynamic contrast-enhanced imaging data, not only dissecting complex tissue into regions with differential tracer kinetics on a pixel-wise resolution but also substantially improving tissue-specific pharmacokinetics parameter estimation (Wang, et al., 2010). CAM-CM is supported by a well-grounded mathematical framework, and combines the advantages of multivariate clustering, convex geometry analysis, and compartmental modeling. The algorithm possesses a novel, powerful feature allowing pure-volume pixels to be readily identified from the measured pixel time series, without any knowledge of the associated compartment pharmacokinetics, leading to a completely unsupervised approach. We provide CAM-CM software as an open-source standalone MATLAB application.

S2 THEORY

We first introduce the typical compartment modeling for analyzing dynamic contrast-enhanced imaging data, and then present the theory of how the tissue compartments can be identified, which gives prime motivations of CAM-CM method.

S2.1 Compartment Modeling

Consider *J*-tissue compartment model for dynamic contrast-enhanced image time series, where the tracer concentration kinetics is governed by a set of linear first-order differential equations (Port, et al., 1999; Roberts, et al., 2006; Tofts, et al., 1999; Zhou, et al., 1997):

$$\frac{dC_1(t)}{dt} = K_1^{In} C_p(t) - k_1^{Out} C_1(t),$$

$$\vdots$$

$$\frac{dC_{J-1}(t)}{dt} = K_{J-1}^{In} C_p(t) - k_{J-1}^{Out} C_{J-1}(t),$$

$$C_{ms}(t) = C_1(t) + \cdots + C_{J-1}(t) + K_p C_p(t),$$

(1)

where $C_j(t)$, $j = 1, 2, ..., J-1$, is the tracer concentration (TC) in the interstitial space weighted by the fractional interstitial volume in the tissue-type j, at time t; $C_p(t)$ is the tracer concentration in plasma (or the plasma input function) and corresponds to the Jth tissue type; $C_{ms}(t)$ is the measured tracer concentration in the region of interest (ROI); K_j^{In} and k_j^{Out} are the wash-in rate and wash-out rate constants in the tissue-type j, respectively; and K_p is the plasma volume in tissue. We acknowledge that there are alternative compartment models that may be more suitable for some particular applications, and we are currently investigating extended methods that can adapt to the alternative compartment models. Equation (1) can be solved for $C_1(t), ..., C_{J-1}(t)$ in terms of the rate constants as

$$C_j(t) = K_j^{In} C_p(t) \otimes \exp(-k_j^{Out} t), \quad j = 1, ..., J-1 \tag{2}$$

where $\otimes$ denotes the mathematical convolution operation.

Let $F_j(t) = C_p(t) \otimes \exp(-k_j^{Out} t)$, $j = 1, 2, ..., J-1$, and $F_J(t) = C_p(t)$. By equations (1) and (2), the spatial-temporal patterns of tracer concentrations in dynamic contrast-enhanced imaging data can be expressed as the following latent tissue-specific compartment model (Wang, et al., 2006):

$$\begin{bmatrix} C_{ms}(i, t_1) \\ C_{ms}(i, t_2) \\ \vdots \\ C_{ms}(i, t_L) \end{bmatrix} = \begin{bmatrix} F_1(t_1) & \cdots & F_{J-1}(t_1) & F_J(t_1) \\ F_1(t_2) & \cdots & F_{J-1}(t_2) & F_J(t_2) \\ \vdots & \cdots & \vdots & \vdots \\ F_1(t_L) & \cdots & F_{J-1}(t_L) & F_J(t_L) \end{bmatrix} \begin{bmatrix} K_1^{In}(i) \\ \vdots \\ K_{J-1}^{In}(i) \\ K_P(i) \end{bmatrix}, \tag{3}$$

at pixel i with $i = 1, ..., N$ (with N being the total number of pixels), where $C_{ms}(i, t_l)$ is the tracer concentration measured at time t_l, $l = 1, 2, ..., L$, L is the number of sampling time points, $K_1^{In}(i), ..., K_{J-1}^{In}(i)$ are the local wash-in constants of the tissue-type 1 to tissue-type J-1, at pixel i, respectively, and $K_p(i)$ is the local plasma volume at pixel i. We should emphasize that our goal is to estimate these (unknown) kinetic parameters $K_1^{In}(i), ..., K_{J-1}^{In}(i), K_p(i)$ and the tissue-specific concentration curves $F_1(t_l), ..., F_J(t_l)$ determined by the parameters $k_1^{Out}, ..., k_{J-1}^{Out}$ from the measurements $C_{ms}(i, t_l)$. Next some realistic conditions on these kinetic parameters will be given, by which the tissue-specific compartments can be shown to be perfectly identifiable.

S2.2 Identifiability of Tissue-specific Compartments

For ease of analysis in the sequel, we normalize $C_{\mathrm{ms}}(i,t)$ and $F_j(t)$ over their effective interval of L time samples via a sum-based normalization that projects the scatter plot data points onto the standard simplex as follows

$$x(i,t_l) = \frac{C_{\mathrm{ms}}(i,t_l)}{\sum_{l'=1}^{L} C_{\mathrm{ms}}(i,t_{l'})}, \quad a_j(t_l) = \frac{F_j(t_l)}{\sum_{l'=1}^{L} F_j(t_{l'})}, \quad l=1,...,L.$$

We then re-express (3) as

$$\mathbf{x}(i) = \begin{bmatrix} \mathbf{a}_1,...,\mathbf{a}_J \end{bmatrix} \mathbf{K}(i), \quad i=1,...,N, \tag{4}$$

where $\mathbf{x}(i) = \begin{bmatrix} x(i,t_1),...,x(i,t_L) \end{bmatrix}^T$, $\mathbf{a}_j = \begin{bmatrix} a_j(t_1),...,a_j(t_L) \end{bmatrix}^T$, $\mathbf{K}(i) = [K_1(i),...,K_J(i)]^T$ is accordingly normalized with $\sum_{j=1}^{J} K_j(i) = 1$. After normalization, the physical meanings of the pharmacokinetics parameters shall be interpreted as the relative local wash-in constants. Since these local wash-in constants and local plasma volume, $\left\{ K_1^{In}(i),...,K_{J-1}^{In}(i), K_p(i) \right\}$ or $\left\{ K_1(i),...,K_J(i) \right\}$, are non-negative, the pixel time series model (4) immediately indicates that the observed pixel time series $\mathbf{x}(i)$ is a non-negative linear combination of the tissue-specific compartment TCs, $\mathbf{a}_1,...,\mathbf{a}_J$, weighted by their spatially-distributed local wash-in constants, $K_1(i),...,K_J(i)$ with $\sum_{j=1}^{J} K_j(i) = 1$. This immediately implies that the observed set of pixel time series $\mathcal{X} = \left\{ \mathbf{x}(1),...,\mathbf{x}(N) \right\}$ is a subset of the *convex hull* of the set of compartment TCs (a convex set readily defined by compartment TCs), $\mathcal{H}\{\mathcal{A}\}$ where $\mathcal{A} = \left\{ \mathbf{a}_1,...,\mathbf{a}_J \right\}$ (Boyd, *et al.*, 2004); that is,

$$\mathcal{X} \subseteq \mathcal{H}\{\mathcal{A}\} = \left\{ \sum_{j=1}^{J} \alpha_j \mathbf{a}_j \mid \mathbf{a}_j \in \mathcal{A}, \ \alpha_j \geq 0, \sum_{j=1}^{J} \alpha_j = 1 \right\}. \tag{5}$$

With (5) in mind, an important question is which conditions are needed to support that the tissue compartment TCs $\mathcal{A}$ can be theoretically identified from the pixel time series $\mathcal{X}$.

Before answering this question, some definitions shall be first introduced as follows (Chen, et al., 2008) (Wang, et al., 2010):

Definition 1. *(Corner points)* A compartment TC $\mathbf{a}_j$ is a corner point of the convex set $\mathcal{H}\{\mathcal{A}\}$ if and only if it can only be expressed as a trivial convex combination of $\mathbf{a}_1,...,\mathbf{a}_J$.

Definition 2. *(Well-grounded points)* Any pixel time course whose associated normalized spatially-distributed wash-in constants are in the form of $\mathbf{K}(i_{\mathrm{WGP}(j)}) = \mathbf{e}_j$ (where $\left\{ \mathbf{e}_j \right\}$ is the standard basis of J-dimensional real space) is called a well-grounded point (WGP) and corresponds to a pure-volume pixel, i.e., $\mathbf{x}(i_{WGP(j)}) = \begin{bmatrix} \mathbf{a}_1,...,\mathbf{a}_J \end{bmatrix} \mathbf{K}(i_{\mathrm{WGP}(j)}) = \mathbf{a}_j$.

The following theorem provides the identifiability of the tissue compartments:

Theorem 1 (Convexity of pixel time series). *Suppose that the J compartment TCs* $\mathbf{a}_1,...,\mathbf{a}_J$ *are linearly independent, and* $\mathbf{x}(i) = \sum_{j=1}^{J} K_j(i)\mathbf{a}_j$ *where non-negative normalized spatially-distributed wash-in constants* $\{\mathbf{K}(i)\}$ *have at least one well-*

grounded point on each of the J coordinate axes, then the convex set specified by $\mathcal{X}$, i.e.,

$$\mathcal{H}\{\mathcal{X}\} = \left\{ \sum\nolimits_{i=1}^{N} \alpha_i \mathbf{x}(i) \mid \mathbf{x}(i) \in \mathcal{X}, \ \alpha_i \geq 0, \ \sum\nolimits_{i=1}^{N} \alpha_i = 1 \right\},$$ *is identical to the convex set*

$\mathcal{H}\{\mathcal{A}\}$, *and its corner points are the J compartment TCs* $\mathbf{a}_1,...,\mathbf{a}_J$.

Proof: By Definition 2 that $\mathbf{x}\left(i_{\mathrm{WGP}(j)}\right) = \mathbf{a}_j$, then for any $\mathbf{z} \in \mathcal{H}\{\mathcal{A}\}$ we have

$$\mathbf{z} = \sum\nolimits_{j=1}^{J} \alpha_j \mathbf{a}_j$$

$$= \sum\nolimits_{j=1}^{J} \alpha_j \mathbf{x}\left(i_{\mathrm{WGP}(j)}\right)$$

$$= \sum\nolimits_{i=1}^{N} \alpha'_i \mathbf{x}(i), \text{ where } \alpha'_i = \begin{cases} \alpha_j, & i \in \left\{i_{\mathrm{WGP}(j)}\right\}, \\ 0, & i \notin \left\{i_{\mathrm{WGP}(j)}\right\}, \end{cases}$$

implying $\mathbf{z} \in \mathcal{H}\{\mathcal{X}\} = \left\{ \sum\nolimits_{i=1}^{N} \alpha'_i \mathbf{x}(i) \mid \mathbf{x}(i) \in \mathcal{X}, \ \alpha'_i \geq 0, \ \sum\nolimits_{i=1}^{N} \alpha'_i = 1 \right\}$, i.e., $\mathcal{H}\{\mathcal{A}\} \subseteq \mathcal{H}\{\mathcal{X}\}$.
On the other hand, for any $\mathbf{z} \in \mathcal{H}\{\mathcal{X}\}$, we have

$$\mathbf{z} = \sum\nolimits_{i=1}^{N} \alpha_i \mathbf{x}(i)$$

$$= \sum\nolimits_{i=1}^{N} \alpha_i \sum\nolimits_{j=1}^{J} K_j(i) \mathbf{a}_j$$

$$= \sum\nolimits_{j=1}^{J} \left[\sum\nolimits_{i=1}^{N} \alpha_i K_j(i) \right] \mathbf{a}_j$$

$$= \sum\nolimits_{j=1}^{J} \beta_j \mathbf{a}_j, \text{ where } \beta_j = \sum\nolimits_{i=1}^{N} \alpha_i K_j(i) \text{ and } \sum\nolimits_{j=1}^{J} \beta_j = 1,$$

implying $\mathbf{z} \in \mathcal{H}\{\mathcal{A}\}$, i.e., $\mathcal{H}\{\mathcal{X}\} \subseteq \mathcal{H}\{\mathcal{A}\}$. Therefore, combining $\mathcal{H}\{\mathcal{X}\} \supseteq \mathcal{H}\{\mathcal{A}\}$ and $\mathcal{H}\{\mathcal{X}\} \subseteq \mathcal{H}\{\mathcal{A}\}$ gives $\mathcal{H}\{\mathcal{X}\} = \mathcal{H}\{\mathcal{A}\}$. Next, we show that $\mathbf{a}_1,...\mathbf{a}_J$ are corner points of $\mathcal{H}\{\mathcal{A}\}$. Since $\mathbf{a}_1,...\mathbf{a}_J$ are linearly independent, we have $\sum\nolimits_{j=1}^{J} \alpha_j \mathbf{a}_j = \mathbf{0}$ iff $\alpha_j = 0 \ \forall j$ which implies that

$$\mathbf{a}_j = \sum\nolimits_{j=1}^{J} \alpha'_j \mathbf{a}_j \text{ iff } [\alpha'_1,...,\alpha'_J]^T = \mathbf{e}_j \ \forall j$$

i.e., $\mathbf{a}_j$ can only be a trivial convex combination of $\mathbf{a}_1,...,\mathbf{a}_J$. By Definition 1, $\mathbf{a}_1,...,\mathbf{a}_J$ are therefore the corner points of convex set $\mathcal{H}\{\mathcal{A}\}$, and together with $\mathcal{H}\{\mathcal{X}\} = \mathcal{H}\{\mathcal{A}\}$, we readily complete the proof of Theorem 1. Q.E.D

The inferences of Theorem 1 are twofold: Firstly, given a set of observed pixel time series, the compartment TCs $\mathcal{A}$ can be identified by searching the corner points of the pixel time series convex set $\mathcal{H}\{\mathcal{X}\}$ when pure-volume pixels exist for each of the tissue compartments (Rijpkema, et al., 2001). Secondly, the pure-volume pixels constitute the corner points of the observed pixel time series convex set, while the partial-volume pixels constitute the interior points of the observed pixel time series convex set.
    One important consideration with the present method is the existence of functionally pure-volume pixels for each of the underlying compartments, and this reasonable assumption reflects only the ideal scenario and constitutes the necessary and sufficient condition for the mathematical identifiability of the signal deconvolution model

(equations (1)-(3)). Also, our CAM-CM solution, introduced in the next section, is proposed to identify the corners of $\mathcal{H}\{\mathcal{A}\}$, *i.e.* the time series of pure-volume pixels, by identifying the corners of $\mathcal{H}\{\mathcal{X}\}$. Nevertheless, it is possible that in some datasets, no pixel is pure and it would be helpful to provide an accurate interpretation of the CAM-CM solution in such non-ideal scenarios. The following theorems show that, if source-dominance pixels exist for each of the underlying tissue compartments, CAM-CM will provide the optimal solution that captures maximum source information (i.e., with the identified corners of the pixel time series scatter simplex corresponding to maximum source-dominance).

Theorem 2 (Source dominance). *Suppose that the non-negative normalized pixel-wise local wash-in rates $K(c_j)=[K_1(c_j),..., K_m(c_j),...,K_J(c_j)]$ are the corners of the pixel time series scatter simplex. Then the CAM-CM solution based on these corners achieves the maximum source dominance in the sense of $K_m(c_j)=\max_{i=1,2,...,N} K_m(i)$.*

Proof of theorem 2. Consider the pixel $\mathbf{K}(i^*)=\alpha_1(i^*)\mathbf{K}(c_1)+\alpha_2(i^*)\mathbf{K}(c_2)+...+\alpha_J(i^*)\mathbf{K}(c_J)$ of the convex hull defined by these corners, whose *m*th entry is the largest among all pixels, i.e., $K_m(i^*)=\max_{i=1,2,...,N} K_m(i)$. Since $\alpha_1(i^*)+\alpha_2(i^*)+...+\alpha_J(i^*)=1$, we may therefore write

$$K_m(i^*)= (\alpha_1(i^*)+\alpha_2(i^*)+...+\alpha_J(i^*))K_m(i^*)=\alpha_1(i^*)K_m(i^*)+\alpha_2(i^*)K_m(i^*)+...+\alpha_J(i^*)K_m(i^*).$$

Alternatively, the *m*th entry of $\mathbf{K}(i^*)$ can be expressed as

$$K_m(i^*)=\alpha_1(i^*)K_m(c_1)+\alpha_2(i^*)K_m(c_2)+...+\alpha_J(i^*)K_m(c_J).$$

By the unique convex expression of $K_m(i^*)$, we have

$$\alpha_1(i^*)[K_m(i^*)-K_m(c_1)]+\alpha_2(i^*)[K_m(i^*)-K_m(c_2)]+...+\alpha_J(i^*)[K_m(i^*)-K_m(c_J)]=0,$$

which, together with the fact $\alpha_1(i^*)\geq 0$ and $K_m(i^*)-K_m(c_j)\geq 0$, implies $i^*=\{c_j\}$.   Q.E.D

The results provided by Theorem 1 and Theorem 2 would allow us to gain further insights beyond the dynamic contrast-enhanced data themselves into how the temporal patterns of the underlying compartment TCs geometrically located at the pixel time series scatter simplex, facilitating the design of separation principle in CAM-CM.

S3 METHODS
As we introduced in the Background section, the CAM-CM method uses *in vivo* dynamic contrast-enhanced imaging data to analyze various functional changes associate with disease initiation, progression and responses to therapy. We herein demonstrate the procedure in the CAM-CM method in **Fig. S1**. Input pixel time courses within the tumor ROI are first normalized onto a simplex and then processed by the following three core components: (1) initialization-free multivariate clustering method that assumes observed pixel time series $\mathcal{X}=\{\mathbf{x}(1),...,\mathbf{x}(N)\}$ follow standard finite normal mixture (SFNM)

model, and aggregates $\mathcal{X}$ into a few clusters by using expectation-maximization (EM) algorithm (Miller, *et al.*, 2003) initialized with affinity propagation clustering (APC) (Frey, *et al.*, 2007), in an attempt to reduce the impact of noise/outlier pixels on model learning; see Section S2.1; (2) convex analysis of mixtures (CAM) that identifies the tissue-specific compartment TCs $\mathbf{a}_1,...,\mathbf{a}_J$ by finding the pure-volume clusters located at the corners of the clustered pixel time series scatter simplex; the details will be given in Section S2.2; and (3) compartment modeling that estimates tissue-specific kinetic parameters $K_1^{In}(i),...,K_{J-1}^{In}(i),K_p(i)$ using only pure-volume pixel time series. See discussion in Section S3.3.
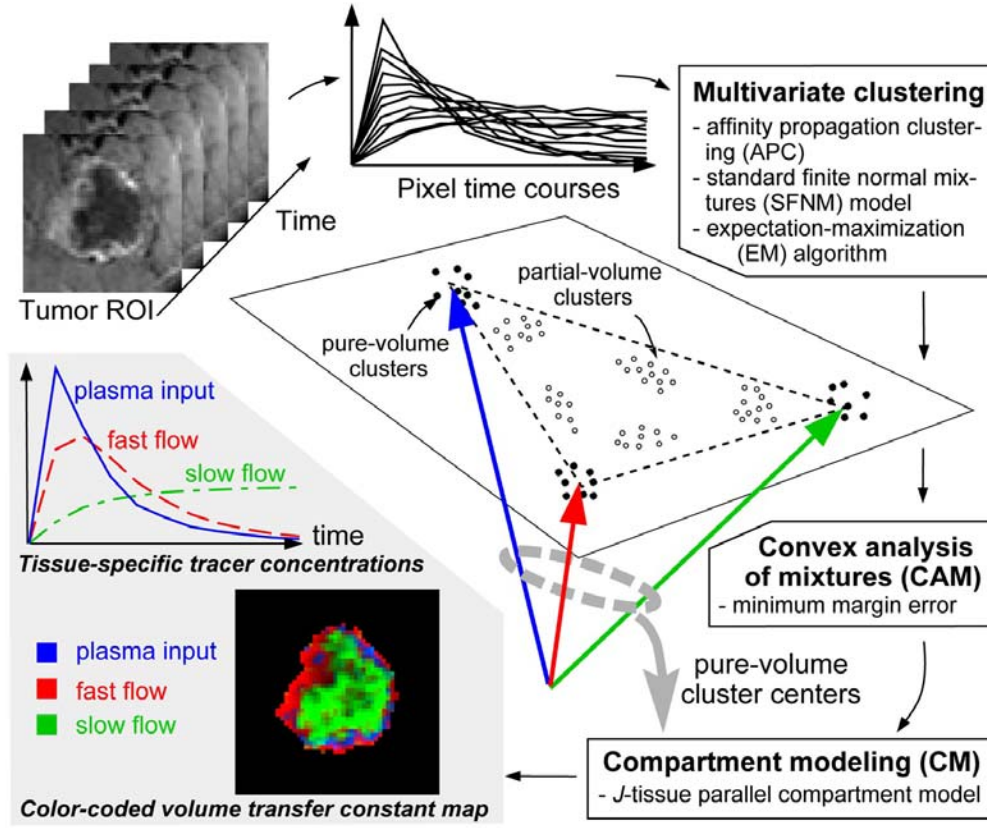

Figure S1. Pictorial flow chart of the CAM-CM method (illustrated on the special case of *J*=3, with three tissue types, "plasma input", "fast flow", and "slow flow", associated with the compartment model (Wang, et al., 2006).

S3.1 Multivariate Clustering of Pixel Time Series

There has been considerable success in using SFNMs to model clustered data sets, such as dynamic contrast-enhanced imaging data (Chen, et al., 2008), taking a sum of the following general form:

$$p\big(\mathbf{K}(i)\big) = \sum\nolimits_{m=1}^{J} \pi_m \, g\big(\mathbf{K}(i) \,|\, \mathbf{e}_m, \boldsymbol{\Sigma}_{\mathbf{K},m}\big) + \sum\nolimits_{m=J+1}^{M} \pi_m \, g\big(\mathbf{K}(i) \,|\, \boldsymbol{\mu}_{\mathbf{K},m}, \boldsymbol{\Sigma}_{\mathbf{K},m}\big), \qquad (6)$$

where the first term corresponds to the clusters of pure volume pixels $(m=1,...,J)$, the second term corresponds to the clusters of partial volume pixels $(m=J+1,...,M)$, M is the total number of pixel clusters, π_m is the mixing factor, $g(\cdot)$ is the Gaussian probability density function, and $\boldsymbol{\mu}_{\mathbf{K},m}$ and $\boldsymbol{\Sigma}_{\mathbf{K},m}$ are the mean vector and covariance matrix of cluster m, respectively. By incorporating (4) into (6), the SFNM model for pixel time series becomes

$$p(\mathbf{x}(i)) = \sum\nolimits_{m=1}^{J} \pi_m\, g\left(\mathbf{x}(i)\,|\,\mathbf{a}_m,\boldsymbol{\Sigma}_{\mathbf{x},m}\right) + \sum\nolimits_{m=J+1}^{M} \pi_m g\left(\mathbf{x}(i)\,|\,\boldsymbol{\mu}_{\mathbf{x},m},\boldsymbol{\Sigma}_{\mathbf{x},m}\right), \qquad (7)$$

where $\boldsymbol{\Sigma}_{\mathbf{x},m} = \mathbf{A}\boldsymbol{\Sigma}_{\mathbf{K},m}\mathbf{A}^T$ and $\boldsymbol{\mu}_{\mathbf{x},m} = \mathbf{A}\boldsymbol{\mu}_{\mathbf{K},m}$, with $\mathbf{A} = [\mathbf{a}_1,...,\mathbf{a}_J]$. Accordingly, the first term of (7) represents the pure volume clusters and the second term of (7) represents the partial volume clusters, and as shown in **Fig. S1** the clustered pixel time series set $\mathcal{X}$ is (approximately) confined within a convex set whose corner centers are the J compartment TCs $\mathbf{a}_1,...,\mathbf{a}_J$.

It has been shown that significant computational savings can be achieved by using the EM algorithm to allow a mixture of the form (7) to be fitted to the data (Chen, et al., 2004; Titterington, et al., 1985). Determination of the parameters of the model (7) can be viewed as a "missing data" problem in which the missing information corresponds to pixel labels $l_{im} = \mathbf{I}(i,m)$ specifying which cluster generated each data point with $\mathbf{I}(i,m)$ denoting the indicator function. If we were given a set of already clustered data with specified pixel labels, then the log likelihood (known as the "complete" data log-likelihood) becomes

$$\mathcal{L}(\mathcal{X}\,|\,\boldsymbol{\Theta},\mathbf{L}) = \sum_{i=1}^{N}\sum_{m=1}^{M} l_{im} \log\left\{\pi_m g\left[\mathbf{x}(i)\,|\,\boldsymbol{\mu}_{\mathbf{x},m},\boldsymbol{\Sigma}_{\mathbf{x},m}\right]\right\}, \qquad (8)$$

where $\boldsymbol{\Theta} = \{\pi_m,\boldsymbol{\mu}_{\mathbf{x},m},\boldsymbol{\Sigma}_{\mathbf{x},m},\forall m\}$ and $\mathbf{L} = \{l_{im}, i=1,2,...,N, m=1,2,...,N\}$. However, we only have indirect, probabilistic information in the form of the posterior responsibilities z_{im} for each model m having generated the pixel time series $\mathbf{x}(i)$. Taking the expectation of (8), we then obtain the complete data log likelihood in the form

$$\mathcal{L}(\mathcal{X}\,|\,\boldsymbol{\Theta},\mathbf{Z}) = \sum_{i=1}^{N}\sum_{m=1}^{M} z_{i,m} \log\left\{\pi_m g\left[\mathbf{x}(i)\,|\,\boldsymbol{\mu}_{\mathbf{x},m},\boldsymbol{\Sigma}_{\mathbf{x},m}\right]\right\}, \qquad (9)$$

where the $z_{i,m} = \Pr\left(l_{im}=1\,|\,\mathbf{x}(i)\right)$ are constants and $\mathbf{Z} = \{z_{i,m}, i=1,2,...,N, m=1,2,...,N\}$.

Maximization of (9) can be performed using the two-stage form of the EM algorithm. At each complete cycle of the algorithm we commence with an "old" set of parameter values $\boldsymbol{\Theta} = \{\pi_m,\boldsymbol{\mu}_{\mathbf{x},m},\boldsymbol{\Sigma}_{\mathbf{x},m},\forall m\}$. We first use these parameters in the E-step to evaluate the posterior probabilities $z_{i,m}$ using Bayes theorem

$$z_{i,m} = \Pr\left(l_{im}=1\,|\,\mathbf{x}(i)\right) = \frac{\pi_m g\left[\mathbf{x}(i)\,|\,\boldsymbol{\mu}_{\mathbf{x},m},\boldsymbol{\Sigma}_{\mathbf{x},m}\right]}{\sum_{m'=1}^{M} \pi_{m'} g\left[\mathbf{x}(i)\,|\,\boldsymbol{\mu}_{\mathbf{x},m'},\boldsymbol{\Sigma}_{\mathbf{x},m'}\right]}, \quad m \in \{1,...,M\}. \qquad (10)$$

These posterior probabilities are then used in the M-step to obtain "new" values $\boldsymbol{\Theta} = \{\pi_m,\boldsymbol{\mu}_{\mathbf{x},m},\boldsymbol{\Sigma}_{\mathbf{x},m},\forall m\}$ using the following re-estimation formulas

$$\pi_m = \frac{1}{N} \sum_{i=1}^{N} z_{i,m} , \tag{11}$$

$$\boldsymbol{\mu}_{\mathbf{x},m} = \frac{\sum_{i=1}^{N} z_{i,m} \mathbf{x}(i)}{\sum_{i=1}^{N} z_{i,m}} , \tag{12}$$

$$\boldsymbol{\Sigma}_{\mathbf{x},m} = \frac{\sum_{i=1}^{N} z_{i,m} \left(\mathbf{x}(i) - \boldsymbol{\mu}_{\mathbf{x},m} \right) \left(\mathbf{x}(i) - \boldsymbol{\mu}_{\mathbf{x},m} \right)^{T}}{\sum_{i=1}^{N} z_{i,m}} . \tag{13}$$

To reduce the likelihood of pixel time series clustering being trapped into local maxima, an effective and initialization-free affinity propagation clustering (APC) is attempted to initialize the parameter $\boldsymbol{\Theta}$ for the EM algorithm and to estimate the number of obtainable clusters (Frey, *et al.*, 2007). We simultaneously consider all data points as potential exemplars (cluster centers) and recursively exchange real-valued messages between data points until a high-quality set of exemplars and corresponding clusters gradually emerges. Let the "similarity" $s(i,m) = -\left\| \mathbf{x}(i) - \mathbf{x}(m) \right\|^2$ indicate how well the data point $\mathbf{x}(m)$ is suited to be the exemplar for data point $\mathbf{x}(i)$; the "responsibility" $r(i,m)$ reflects the accumulated evidence for how well-suited data point $\mathbf{x}(m)$ is to serve as the exemplar for data point $\mathbf{x}(i)$, and the "availability" $a(i,m)$ reflects the accumulated evidence for how appropriate the data point $\mathbf{x}(i)$ chooses data point $\mathbf{x}(m)$ as its exemplar. Then, the responsibilities $r(i,m)$ are computed based on

$$r(i,m) \leftarrow s(i,m) - \max_{m' \neq m} \left\{ a(i,m') + s(i,m') \right\} , \tag{14}$$

where the availabilities $a(i,m)$ are initialized to zero and the competitive update rule (14) is purely data-driven. Whereas the responsibility update (14) allows all candidate exemplars to compete for ownership of a data point, the availability update rule

$$a(i,m) \leftarrow \min \left\{ 0, r(m,m) + \sum_{i' \notin \{i,m\}} \max \left\{ 0, r(i',m) \right\} \right\} \tag{15}$$

collects evidence from data points to support a good exemplar, where the "self-availability" is updated differently

$$a(m,m) \leftarrow \sum_{i' \notin m} \max \left\{ 0, r(i',m) \right\} . \tag{16}$$

At any iteration during affinity propagation, availabilities and responsibilities are combined to identify exemplars and to terminate the algorithm when these decisions do not change for 10 iterations (Frey, *et al.*, 2007). One advantage of APC is that the number of clusters need not be specified a priori but emerges from the message-passing procedure and only depends on the density distribution of the data points and a parameter. The preference associated with similarities *s(k,k)* for all data points can be taken as input of APC, and can be varied to produce different number of clusters. The shared value could be the median of the input similarities (resulting in a moderate number of clusters) or their minimum (resulting in a small number of clusters). We use the median of the

input similarities in our experiments, which enables automatic model selection on *M* (Frey*, et al.*, 2007).

S3.2 Convex Analysis of Mixtures

Suppose that the *M* cluster centers $\mathbf{\mu}_{\mathbf{x},1},...,\mathbf{\mu}_{\mathbf{x},M}$ were obtained by the APC-SFNM-EM method. As theoretically supported by Theorem 1, CAM can estimate the compartments by detecting the most probable *J* corner clusters of the convex hull containing all clusters of pixel TCs. Assuming the number of compartments *J* is known a priori, an exhaustive combinatorial search (with total C_J^M combinations) is used to find the compartments $\left\{\mathbf{\mu}_{\mathbf{x},m_1},...,\mathbf{\mu}_{\mathbf{x},m_J}\right\}$ (any subset of $\left\{\mathbf{\mu}_{\mathbf{x},1},...,\mathbf{\mu}_{\mathbf{x},M}\right\}$) based on a minimum-error-margin convex-hull-to-data fitting criterion. The margin (*i.e.*, distance) between $\mathbf{\mu}_{\mathbf{x},m}$ and the convex hull $\mathcal{H}\left\{\mathbf{\mu}_{\mathbf{x},m_1},...,\mathbf{\mu}_{\mathbf{x},m_J}\right\}$ is computed by

$$\delta_{m,(m_1,...,m_J)} = \min_{\alpha_{m_1}...\alpha_{m_J}} \left\| \mathbf{\mu}_{\mathbf{x},m} - \sum_{j=1}^J \alpha_{m_j}\mathbf{\mu}_{\mathbf{x},m_j} \right\|_2, \tag{17}$$

where $\alpha_{m_j} \geq 0$ and $\sum_{j=1}^J \alpha_{m_j} = 1$. It shall be noted that if $\mathbf{\mu}_{\mathbf{x},m}$ is inside $\mathcal{H}\left\{\mathbf{\mu}_{\mathbf{x},m_1},...,\mathbf{\mu}_{\mathbf{x},m_J}\right\}$ then $\delta_{m,(m_1,...,m_J)} = 0$. Next, we define the convex-hull-to-data fitting error as the sum of the margin between the convex hull and the "exterior" cluster centers and detect the most probably *J* corners with cluster indices $\left(m_1^*,...m_J^*\right)$ when the criterion function reaches its minimum:

$$\left(m_1^*,...m_J^*\right) = \arg\min_{(m_1,...,m_J)} \sum_{m=1}^M \delta_{m,(m_1,...,m_J)}. \tag{18}$$

The optimization problems of (17) and (18) can be solved by advanced optimization method, such as sequential quadratic programming (SQP) (Boyd*, et al.*, 2004), and an exhaustive combinatorial search (for realistic values of *J* and *M*, in practice), respectively. The principle of (17) and (18) is illustrated by **Fig. S2**, where given a set of points the fitted convex hull with minimum error margin will be chosen.
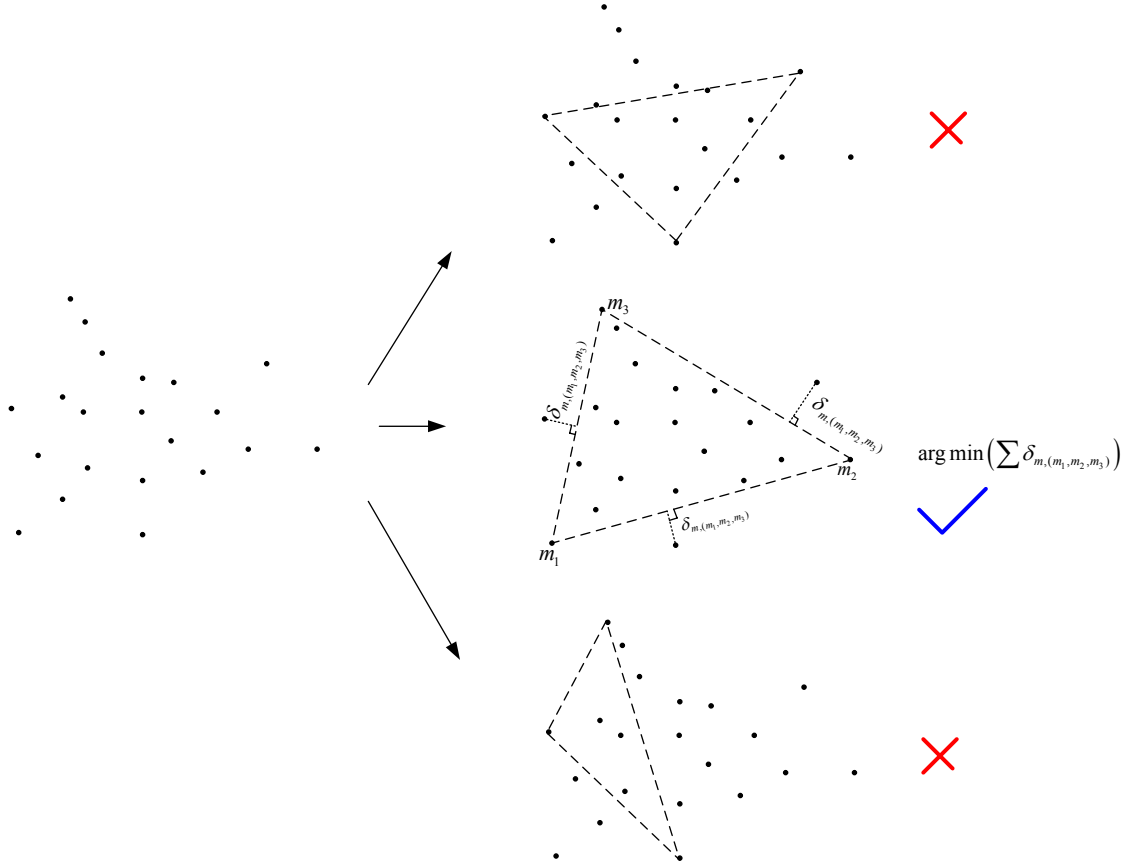
Figure S2. Principle of minimum-error-margin criterion.

S3.3 Tissue-specific Compartment Analysis

Having determined the probabilistic pixel memberships associated with the pure-volume compartments, $\left\{z_{1,m_j^*},...,z_{N,m_j^*}\right\}$ for $j=1,...,J$ by APC-SFNM-EM and CAM methods, we can directly estimate the cluster of different tissue types from the dynamic contrast-enhanced image pixel time series $C_{ms}(i,t_l)$ as follows:

$$C_j(t_l) = \frac{\sum_{i=1}^N z_{i,m_j^*} C_{ms}(i,t_l)}{\sum_{i=1}^N z_{i,m_j^*}}, \quad j=1,...,J, \quad l=1,...,L. \tag{19}$$

It can be known from (1)-(3) that there exists one tissue type called plasma input function $C_p(t_l)$ which is a crucial factor in estimating the tissue-specific kinetic parameters $K_1^{In}(i),...,K_{J-1}^{In}(i), K_p(i)$. Based on widely accepted biological knowledge, we first specify the cluster associated with the plasma input among $C_1(t_l),...,C_J(t_l)$ by selecting the one with fastest wash-in and wash-out rates; for instance, the Jth cluster is selected without loss of generality $C_p(t_l) = C_J(t_l)$. Moreover, we rewrite (2) in the form of discrete acquisition with temporal resolution Δt (/min) as below

$$C_j(t_l) = K_j^{In}\Delta t\, C_p(t_l) \otimes \exp(-k_j^{Out}t_l), j=1,...,J-1, \tag{20}$$

where the *J-1* clusters $\left\{ C_1(t_l),...,C_{J-1}(t_l) \right\}$, the plasma input $C_p(t_l)$ and temporal resolution Δt are given. Hence, the wash-in and wash-out rate constants, K_j^{In} and k_j^{Out} , can be estimated by solving the following minimum-sum-square-errors optimization problem

$$\left\{ \hat{K}_j^{In}, \hat{k}_j^{Out} \right\} = \arg \min_{K_j^{In}, k_j^{Out}} \sum_{l=1}^{L} \left(C_j(t_l) - K_j^{In}\Delta t \, C_p(t_l) \otimes \exp(-k_j^{Out}t_l) \right)^2$$

$$\text{s.t.} \quad K_j^{In} \geq 0, k_j^{Out} \geq 0$$

(21)

for $j = 1,...,J-1$. Since $\left\{ \hat{K}_j^{In}, \hat{k}_j^{Out} \right\}$ only reflect representative kinetic values for the *j*th pure-volume cluster, to shed some light on the spatial heterogeneity of vascular permeability (Zhou, et al., 1997), based on (3), we can further estimate the local wash-in constants $\mathbf{K}_{local} = \left[K_1^{In}(i),...,K_{J-1}^{In}(i), K_p(i) \right]^T$ by solving the following optimization problem:

$$\hat{\mathbf{K}}_{local}(i) = \arg \min_{\mathbf{K}_{local}(i)} \sum_{l=1}^{L} \left(C_{ms}(i,t_l) - \left[\hat{F}_1(t_l),...,\hat{F}_J(t_l) \right] \mathbf{K}_{local}(i) \right)^2$$

$$\text{s.t.} \quad K_p(i) \geq 0, \, K_j^{In}(i) \geq 0, j = 1,...,J-1$$

(22)

where $\hat{F}_j(t_l) = \Delta t \, C_p(t_l) \otimes \exp(-\hat{k}_j^{Out}t_l)$, $j = 1,...,J-1$ and $\hat{F}_J(t_l) = C_P(t_l)$. Eventually, the local wash-in constant maps can be constructed by solving (22) for $i = 1,...,N$. Again, the problems (21) and (22) can be efficiently handled by SQP.

S4 SOFTWARE DEVELOPMENT

To facilitate the use of CAM-CM algorithm, we have developed a MATLAB software package for different application scenarios in dynamic contrast-enhanced imaging. The software package contains two main functions, namely CAM and CM, that implement the CAM-CM method. The software package is constructed using MATLAB common operations, and various functions for performing convex optimization, multivariate clustering, deconvolution, and supervised linear projection. Although our software package is mainly for implementing CAM-CM, the functions for convex optimization, multivariate clustering, and supervised linear projection can be freely extended to other applications.

S4.1 CAM-CM software

Before using CAM-CM software, users need to do the following three things:
(1) Set the CAM-CM folder as the "current directory" of MATLAB.
(2) Add the CAM-CM folder and its subfolders as MATLAB paths by clicking "File"-"Set Path"-"Add with Subfolder" on MATLAB main menu, in order to allow CAM-CM to call the required functions.
(3) Make sure that MATLAB has the optimization toolbox installed.
     The CAM-CM software takes as input the .mat data files that record the pixel time series of the dynamic contrast-enhanced images in matrices. Each row corresponds to a time frame and each column corresponds to a pixel. The CAM-CM contains three

sub-procedures: (1) an initialization-free multivariate clustering method, APC, is applied with the author-suggested parameter setting; i.e., median of the input similarities (resulting in moderate number of clusters) (Frey*, et al.*, 2007); (2) taking APC exemplars as the initialization of cluster centers, the EM algorithm is then performed to cluster pixel time series under a SFNM model; (3) a novel convex hull algorithm, based on the minimum-error-margin criterion, is performed to identify the pure-volume cluster centers as compartment TCs. Given the measured TCs and the estimated compartment TCs, CM is then performed to estimate the tissue-specific kinetic parameters. The outputs of CAM-CM software include not only the numerical records for tissue-specific TCs and pharmacokinetic parameters estimates, but also a multiplatform graphical summary that includes compartment TCs, convexity-preserved clustered scatter simplex, and dissected and composite compartment parametric images. The systematic flowchart of CAM-CM software is given in **Fig. S3**.
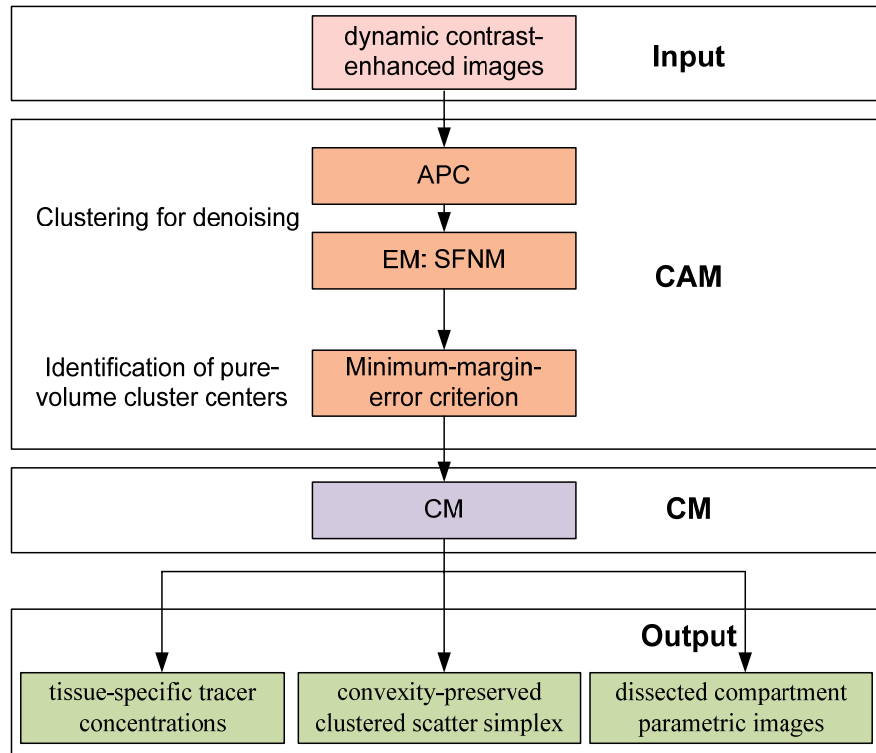

Figure S3. The systematic flow chart of CAM-CM software

Running CAM-CM software is automatic and convenient, with only two user-controlled parameters: the number of tissue types/compartments (J) and the sampling time interval between two consecutive dynamic image frames (Δt). We also provide two options for users to decide whether the denoising procedure and visualization of convexity is needed or not.

There are three files and three folders within the root directory of CAM-CM software. The three files are "CAM.m", "CM.m" and a readme file, and the three folders are "\docs\", "\functions\", and "\simulation data\". "CAM.m" and "CM.m" are the main functions to perform CAM-CM method on contrast-enhanced dynamic imaging data, and both CAM.m and CM.m call the functions under the folder "\functions\". Folder "\docs\"

includes a descriptive document. The other folder, "\simulation data\", provides examples on how to use the CAM function and CM function. The experimental results of these examples are stored in the same folde.

CAM is to find the J corner points of a convex hull formed by the given data X. The syntax of CAM function is:

$$[A\_est\ S\_est] = CAM(X, J, denoise, vis),$$

where the inputs are:

X   - M × N matrix where M is the number of image time frames, and N is the number of pixels; ROI-outlined dynamic imaging data, each column is the measured TC curve of a pixel in the ROI.

J - the number of organs/tissues (or compartments) to be extracted (maximally 10).

denoise   - the option for whether multivariate clustering is used to denoise (denoise=1) or not to denoise (denoise=0) the raw data. In our experiments, we set denoise=1 for DCE-MRI, and denoise=0 for optical imaging.

vis   - visualization of the convexity-preserved simplex (if denoise=1).

and the outputs are:

A_est   - M × K matrix; the tracer/contrast concentration of the major organs

S_est   - K × N matrix; estimated spatial distribution maps of the organs/tissues/compartments.

CM is to estimate wash-in and wash-out rates for J-tissue compartment model. The syntax of CM function is:

$$[eKtrans, eKep, pixelwise\_Ktrans]=CM(X, TCs, initk, del\_t),$$

where the inputs are:

X   - M × N matrix where M is the number of image time frames, and N is the number of pixels; ROI-outlined dynamic imaging data, each column is the measured TC curve of a pixel in the ROI.

TCs   - the estimated tracer/contrast concentration from CAM, *i.e.*

$$\begin{bmatrix} F_1(t_1) & \cdots & F_{J-1}(t_1) & F_J(t_1) \\ F_1(t_2) & \cdots & F_{J-1}(t_2) & F_J(t_2) \\ \vdots & \cdots & \vdots & \vdots \\ F_1(t_L) & \cdots & F_{J-1}(t_L) & F_J(t_L) \end{bmatrix}$$

initk   - the initialization for kinetic parameters $\begin{bmatrix} K_1^{In}(i) & k_1^{Out}(i) \\ K_2^{In}(i) & k_2^{Out}(i) \\ ... \\ K_{J-1}^{In}(i) & k_{J-1}^{Out}(i) \end{bmatrix}$

del_t   - the time interval between consecutive dynamic images.

and the outputs are:

eKtrans   - estimated compartmental wash-in constants, *i.e.*

$$\left[K_1^{In}(i), K_2^{In}(i),..., K_{J-1}^{In}(i) \right]$$

eKep   - estimated compartmental wash-out constants, *i.e.*

$$\left[k_1^{Out}(i), k_2^{Out}(i), ..., k_{J-1}^{Out}(i) \right]$$

pixelwise_Ktran - pixel-wise wash-in constants.

S4.2 MATLAB library for convex optimization, clustering and dimension reduction

The MATLAB library is under the folder "\functions\". The library has 10 functions, among which 3 self-written functions are the key components of CAM-CM framework, and can be readily used for other purposes.

(1) measure_conv: to identify vertices of a convex hull that best confines a set of points, based on the minimum-error-margin criterion (see equation (18)). It takes two inputs: i) the data matrix "X" with each column corresponding to a data point and each row corresponding to a variable; ii) the number of corner points of this convex hull "*N*". The outputs are i) "*eA*" – the estimated corner points, where each column is a corner point; ii) "*cornerind*" – the index of these corner points in the data matrix "X".

(2) SL_EM: EM algorithm to solve the SFNM (see equation (7)). It takes 6 inputs and 7 outputs. Details for the parameters can be found in the .m file. Here we briefly describe the 4 important inputs and some important outputs. The 4 inputs include i) "*y*", the input data, where each column is a sample; ii) "*estmu*", the initialization of cluster center, where each column is a center; iii) "*estcov*", the initialization of covariance matrix; iv) "*estpp*", the initialization of prior probability of each cluster. Among the outputs, there are also "*estmu*", "*estcov*", "*estpp*", but they are estimates instead of initializations. Also, "*normindic*" records the estimated posterior probability that a data point belongs to a cluster, with each column corresponding to a data point.

(3) nnls: nonnegative least-squares fitting to estimate the wash-in and wash-out constants from the measured TCs and the compartment TCs (see equations (21) and (22)). The input "X" is the data matrix (mixture), with each column being a data point, the input "A" is the mixing matrix, and the output "S" is the estimated source signal.

S4.3 Simulation Study and Validation

The "Simulator and data\demo_for_simulation.m" gives an example of the CAM-CM analysis on a dynamic contrast-enhanced magnetic resonance imaging (DCE-MRI) simulation dataset based on three-tissue compartments (*J*=3), including plasma input, tissue with slow tracer kinetics (fast-flow compartment), and tissue with slow tracer kinetics (slow-flow compartment). The dataset can be found under directory "\Simulation data\".

We provide twelve simulated datasets corresponding to four different ground truth kinetic parameter settings (scenarios) and three different signal-to-noise ratios (SNRs) in ".mat" files under directory "Simulation data\". For example, "simdataS1SNR10.mat" denotes the case under scenario 1 and SNR=10. The ground truth kinetic parameter values in every scenario can be found in the .mat files. Users can select scenarios and SNRs, and simulate as many datasets as needed via "Simulation data\simulator.m".

Each simulated dataset is stored together with the associated ground truths defined below:

gtTCf gtTCs gtTCp - ground truth tracer concentration of plasma input, fast-flow and slow-flow compartments.

Ktrans_f	- ground truth compartmental wash-in constant for fast-flow compartment.
Kep_f	- ground truth wash-out constant for fast-flow compartment.
Ktrans_s	- ground truth compartmental wash-in constant for slow-flow compartment.
Kep_s	- ground truth wash-out constant for slow-flow compartment.
del_t	- temporal sampling interval (min).
gtSp, gtSf, gtSs	- ground truth partial volume weights for plasma input, fast-flow and slow-flow compartments.

Now we demonstrate the results of CAM-CM on the dataset, "\Simulation data\simdataS1SNR10.mat": please open "\Simulation data\demo_for_simulation.m" and click "Run" button in MATLAB editor window. CAM-CM will be run on the simulated dynamic imaging data "simdataS1SNR10" and return the estimated quantities described in section 2. "demo_for_simulation.m" saves the estimated kinetic parameters along with their ground truth counterparts under "\Simulation data\ "; it also saves the estimated TCs and their ground truth counterparts in the figure files "estimated TCs.jpg" and "ground truth TCs.jpg", respectively, under "\Simulation data\".

For example, for the dataset generated with SNR=10 under scenario 1, "simdata_S1SNR10", the estimates of kinetic parameters are stored in the file "simresult.mat". Here we compare the ground truth kinetic parameters and their estimated values by CAM-CM in **Table S1**. The results show a good performance of CAM-CM for the noisy case.

Table S1. The ground truth kinetic parameters and CAM-CM estimates for SNR=10dB.

	K_f^{In} (/min)	k_f^{Out} (/min)	K_s^{In} (/min)	k_s^{Out} (/min)
Ground truth	0.0300	0.5000	0.0300	0.1000
CAM-CM estimates	0.0296	0.4875	0.0296	0.0963

The results can be further demonstrated by comparing the estimated TCs with the ground truth TCs. **Fig.S4** shows the estimated compartment TCs when testing CAM-CM on "simdata_S1SNR10".

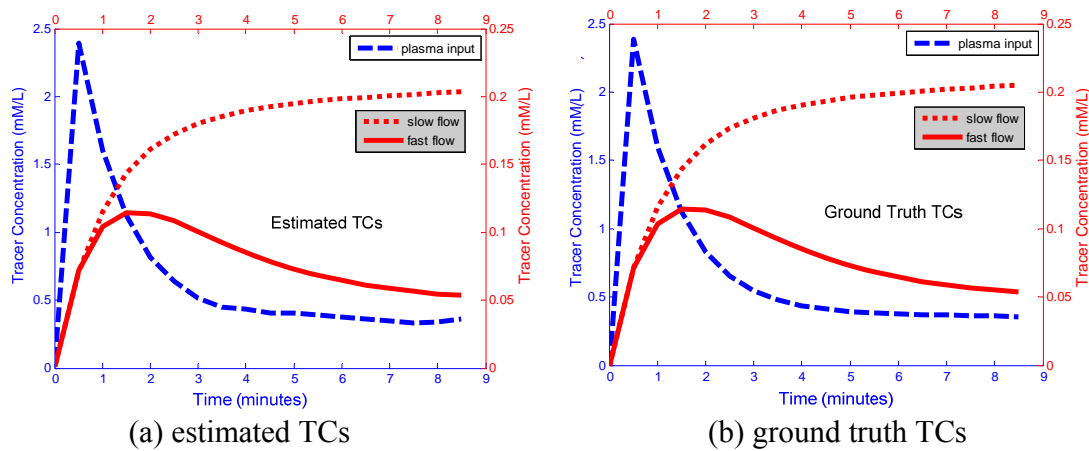(a) estimated TCs   (b) ground truth TCs

Figure S4 The ground truth TCs and their estimates by CAM-CM software. We used two Y-axes in each figure, to visualize the TCs with different scales. Note that the TCs for slow flow and fast flow follow the "red Y-axis" on the right while the TC for plasma input follows the "blue Y-axis" on the left.

S5 CASE STUDIES

As aforementioned, classic compartment modeling methods are oblivious to tissue heterogeneity. They can neither distinguish between variations in kinetic patterns resulting from actual physiological changes versus differences in tissue-type composition, nor identify the contributions of different compartments to the total measured tracer concentration. Therefore, their power to detect mechanistic change of kinetic patterns could be significantly confounded by variations under different tissue-type compositions (McDonald, *et al.*, 2003; Padhani, *et al.*, 2001).

CAM-CM can dissect complex tissues into regions with differential tracer kinetics on a pixel-wise resolution, and thus provide a systems biology tool for defining imaging signatures predictive of phenotypes. In this section, we introduce the tissue-specific kinetic pattern dissection, performed by CAM-CM, on realistic dynamic imaging cases.

S5.1 A case study on DCE-MRI

We first considered a T1-weighted gadolinium-enhanced (Gd-DTPA) DCE-MRI dataset (collected by Dr. Choyke, NIH Clinical Center) of an advanced breast cancer case (Choyke, et al., 2003; Turkbey, et al., 2010) (**Fig. S5**). The three-dimensional DCE-MRI scans were performed every 30 seconds for a total of 11 minutes after the injection, on a 1.5 Tesla magnet using three-dimensional spoiled gradient-echo sequences (TR < 7 msec, TE < 1.5 msec, flip angle = 30°, matrix = 192 × 256, 0.5 averages). Typically, 12-15 slices are obtained and 15-18 time frames are acquired for each case.

The application of compartment model in this case study uses a three-tissue model with $J=3$ accounting for fast, slow, and plasma input compartments (Wang, et al., 2006). Our CAM-CM analysis reveals two biologically interpretable compartments with distinct physiological kinetic patterns (**Fig. S5c**): (1) Fast-flow: fast clearance rate of the tracer; (2) Slow-flow: very slow tracer kinetics. They are associated with local wash-in constant maps with different spatial distributions (**Fig. S5d**): (1) Fast-flow: peripheral "rim" region of the tumor; (2) Slow-flow: inner "core" region of the tumor. As can be expected, the overlap of regions (partial volume pixels) that was noticed on these maps cannot be obtained in the ROI studies. Our analysis indicates that the tumor site contains a significant fraction (84.3%) of partial volume pixels, which can be visually observed from and verified by the "filled" three-corner convex hull of the projected pixel time series scatter plot (**Fig. S5a**). As shown by the dissected and overall TC dynamic patterns (**Fig. S5c** versus **S5b**), the values found for the kinetic parameters by CAM-CM demonstrate that the tumor site contains rapid and slow tracer clearance compartments and estimated $\mathbf{K}^{In}(i)$ varies from pixel to pixel, which otherwise could not be seen if tissue heterogeneity was not taken into account (Padhani, *et al.*, 2001).
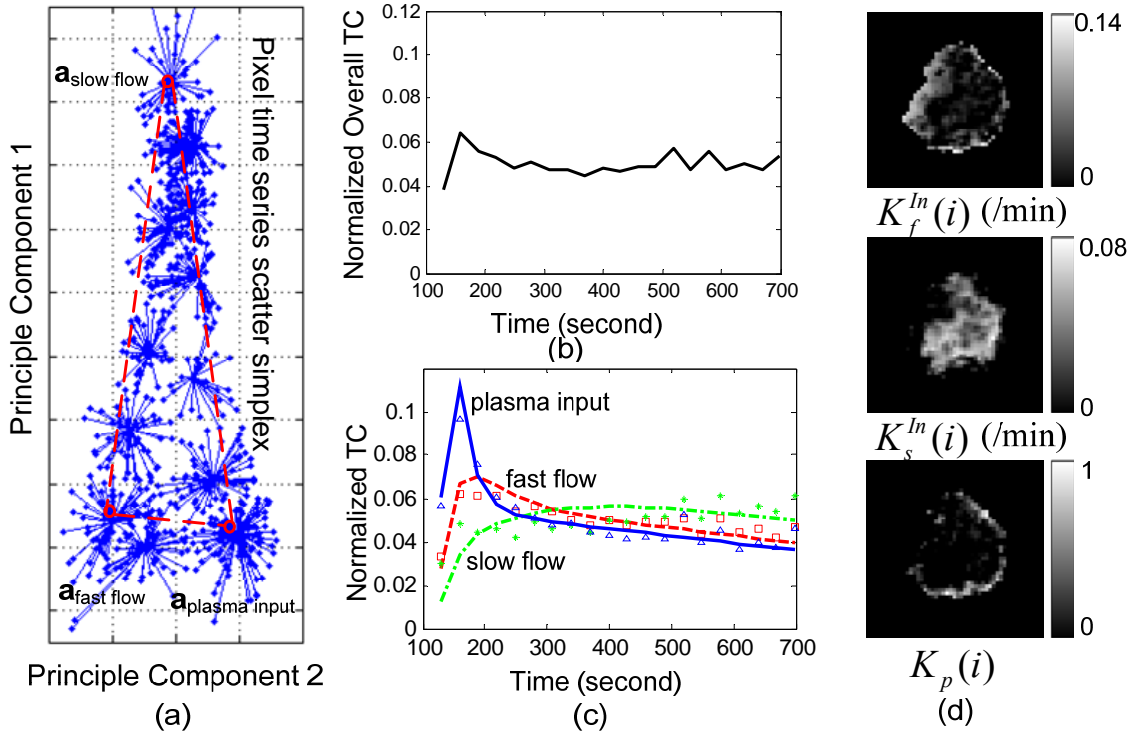
Figure S5. The experimental results of CAM-CM on a typical breast cancer DCE-MRI data. (a): The identified convex hull of clustered pixel TCs (Blue dots: normalized pixel TCs; Red circles: cluster centers; Blue lines: cluster memberships). (b): Normalized overall TC calculated from the entire tumor ROI. (c): Normalized compartment TCs estimated by CAM-CM (the discrete curves show the normalized TCs directly estimated via CAM; while the smooth curves show the normalized TCs which are fitted by the kinetic parameters estimated via CAM-CM). (d): Local wash-in constant maps estimated by CAM-CM. The physical meanings of $K_f^{In}(i)$ and $K_s^{In}(i)$ refer to the local wash-in constants associated with tissue compartments of fast flow and slow flow in the compartment model, and $K_p(i)$ denotes the local volume of plasma input.

The outcomes of CAM-CM analysis are plausibly consistent with the previously reported heterogeneity within tumors (Choyke, *et al.*, 2003; Costouros, *et al.*, 2002; McDonald, *et al.*, 2003; Padhani, *et al.*, 2001). Since angiogenesis is essential to tumor development, it has been widely observed that active angiogenesis in advanced breast tumors often occurs in the peripheral "rim" with co-occurrence of inner-core hypoxia (McDonald, *et al.*, 2003; Yankeelov, *et al.*, 2007). Defective endothelial barrier function due to vascular endothelial growth factor (VEGF) expression is one of the best-documented abnormalities of tumor vessels, resulting in spatially heterogeneous high microvascular permeability to macromolecules (Choyke, *et al.*, 2003; McDonald, *et al.*, 2003; Padhani, *et al.*, 2001). Specifically, tumor neovasculature is *abnormal* – leaky vessels, chaotic and tortuous structure, and dead ends, giving rise to a rapid enhancement and gradual washout pattern (Choyke, et al., 2003). At the same time, as a tumor grows, it rapidly outgrows its blood supply and requires neovessel maturation, leaving an inner core of the tumor with regions where the blood flow and oxygen concentration are

significantly lower than in normal tissues, gives rise to a much slower accumulation and minimum washout pattern (Brown*, et al.*, 2004; Choyke*, et al.*, 2003). In fact, the estimated $\mathbf{K}^{In}(i)$ maps reveal regions of differential function that correlate with differential gene expression involved in angiogenesis (Choyke, et al., 2003; Costouros, et al., 2002). Furthermore, the CAM-CM estimated values of $k_f^{Out} = 1.14$ min^{-1} and $k_s^{Out} = 0.37$ min^{-1} were generally consistent with the parameter values reported by the most relevant studies (Knopp, et al., 1999).

S5.2 A case study on dynamic fluorescence image data

We then considered a case study on dynamic fluorescence molecular imaging of a small animal. Fluorescence molecular imaging has great potential for advancing basic research and drug discovery and development, but widespread adoption of optical imaging modality is being held back because of obstacles to truly quantitative imaging of deeper organs, tissues, and targets (Hillman*, et al.*, 2007). Applying CAM-CM method to the dynamic fluorescent image data of a small mouse can automatically identify and locate the internal organ or structure from which a molecular signal may have originated, and provide the biodistribution dynamics of the major organs, which can facilitate versatility for studies of orthotropic disease, diagnostics and therapies.

Two dynamic fluorescence image data sets of a small mouse in a supine and prone positions, provided by Dr. Hillman (Hillman*, et al.*, 2007), were acquired after bolus injection of a mixture of indocyanine green (ICG) and digital tissue recognition (DTR) (Hillman*, et al.*, 2007): ten image series (50 ms integration time per frame) were scanned every two seconds for each excitation/emission pair for up to 40 min, and each group of 10 successive images was averaged to create a sequence of 316 images (for prone position) and 256 images (for supine position) with four seconds between each. Since the two datasets were acquired by switching optical filters to capture signal from each dye separately, only the data capturing the ICG dye is included in our analysis. ICG dye begins by circulating through the mouse's vascular system, and then either accumulates in different tissues, or clears from them. ICG quickly binds to albumin and is cleared through the liver. The dyes used are not 'stains' per se, but interact in characteristic ways with each organ, and therefore result in each organ having a distinctive temporal pattern of dye wash-in and wash-out. These dynamics are what our CAM-CM algorithm exploits to extract both the organ-specific dynamics, as well as a map that clearly delineates each organ. Some preprocessing, such as image registration (due to the camera moved slightly), and image sides amplification also have been applied to the two datasets to improve the results of the subsequent CAM-CM analysis.

Due to the image-average strategy that eliminates the noise contaminations and the high similarity of biodistribution dynamics associated with the major organs, the first component of CAM-CM method, namely multivariate clustering, was not employed for these datasets. In addition, the third component of CAM-CM method, namely tissue specific compartment modeling, relies on a plasma input function to estimate the representative wash-in constants for different organs. Since the plasma input function is not available throughout the optical image data, we constructed an estimated plasma input function using a well-adopted population average method (Yang, et al., 2007). Unlike DCE-MRI dataset that generally involve less than 25 image time series, the

optical image data contain 316 images for prone position mouse and 256 images for supine position mouse can be a huge computational burden in our CAM-CM analysis. We have chosen to adopt the well-known "feature extraction" scheme using principal component analysis (PCA) (Bishop*, et al.*, 1998; Haykin, 1999; Hillman*, et al.*, 2007). Although there is no theoretically agreed optimum number of retained principal components across various applications, a popular approach is to evaluate the retained percentage of variability (Hastie, et al., 2009). In this case study, we have found that the top 20 principal components can preserve more than 95% of the total variability in the original data, and hence we set the number of preserved dimensions 20 for the two datasets. Our experience has shown that PCA-based dimension reduction can lead to more accurate and efficient performance of the CAM-CM analysis.

Results of applying CAM-CM to the prone position data set (with setting the number of major organs to $J=10$) were physiologically interpretable (**Fig. S6a-c**). Ten fluorescent time courses (**Fig. S6a**) show distinct patterns of circulating, accumulating or metabolizing of the dye in different organs, and plausibly coincide with the expected physiological trends, such as late uptake by adipose tissue and fast disappearance from the brain region. The estimated kinetic parameters for different organs (**Table S2**) also reflect the expected physiological accumulating and metabolizing rates of the dye. The merged and color-coded spatial maps (**Fig. S6b**) also constitute an anatomical structure of the mouse that exhibits a high agreement with the results in (Hillman*, et al.*, 2007) and their comparison to true anatomy, allowing the longitudinal identification of the internal organs. The individual spatial maps (**Fig. S6c**) also achieve correct localization of the major organs in most cases. Additional structure indicates that these regions also have similar dynamic behavior to the organ. On the supine position data set, CAM-CM analysis (with setting the number of major organs equal to $J=5$) is also able to capture the physiologically meaningful behavior of each organ (**Fig. S7a-c**). For instance, a sustained uptake by the liver can be easily observed (**Fig. S7a**). Once again, the merged and color-coded spatial maps are consistent with the results in (Hillman*, et al.*, 2007) (**Fig. S7b-c**), and the estimated kinetic parameters follow physiological accumulating and metabolizing rates of the dye in different organs (**Table S3**). Note that the notable differences in the estimated kinetic parameters between the supine (**Table S2**) and the prone position (**Table S3**) are not mainly attributable to the CAM-CM software, but rather to the different origins of the data — these data were acquired (and/or) at different times, on different mice, under different conditions, and with different positions.

It is also important to emphasize the benefits of optical imaging over, for example computed tomography: Firstly, optical imaging of small animals is a powerful tool for basic research and pharmaceutical development in which targeted dyes or more recently fluorescent proteins or luminescence are used to label tumors or other cells or organs for longitudinal measurement of the effects of therapies or interventions. Such imaging systems typically produce 'zero-background' images where labeled cells are seen against a dark background of unlabeled organs, making it very difficult to determine the anatomical location of the labeled tissues. While X-ray CT could provide a 3D map of the internal organs of the mouse, it is an expensive system that requires shielding and is almost impossible to combine with optical imaging, which otherwise requires a fairly inexpensive bench-top box for image acquisition. Our approach for dynamic imaging to map the organs of the mouse requires no modifications to conventional optical imaging

hardware apart from acquisition of a time-series of images instead of a static image, and a small bolus injection of a dye. Anatomical maps produced are exactly co-registered with the position of the animal, and are in the same imaging geometry and with the same image distortions as imaging of a targeted dye or labeled region. Currently, this approach has been implemented, but requires the user to interact with the unmixing step of generating anatomical maps (Hillman*, et al.*, 2007). Our CAM-CM approach makes this into a completely automated step. Beyond development of anatomical maps, dynamic optical imaging is now being explored to look at differences in perfusion or dye uptake dynamics in diseased tissues, as an alternative to using specifically targeted dyes. A further use is to label substances of interest such as drugs and nutrients and to use dynamic optical imaging to explore the biodistribution and pharmacokinetic dynamics of these substances in real time. No equivalent techniques are available for this kind of analysis in-vivo. Again, CAM-CM would be able to find both the location of different organs, and the characteristic dynamics of the labeled substances in each of those organs, providing objective analysis for high through-put longitudinal studies.

Table S2. Estimated kinetic parameters for the prone position data.

	Kid-ney	Spine	Adi-pose	Large intestine	Nodes	Blood vessels	Liver	Brain	Spl-een	Lung
K_j^{In}	1.000	1.027	0.733	0.781	0.672	0.989	0.784	0.755	0.896	0.666
k_j^{Out}	0.013	0.024	0.010	0.020	0.005	0.022	0.013	0.026	0.014	0.017

Table S3. Estimated kinetic parameters for the supine position data.

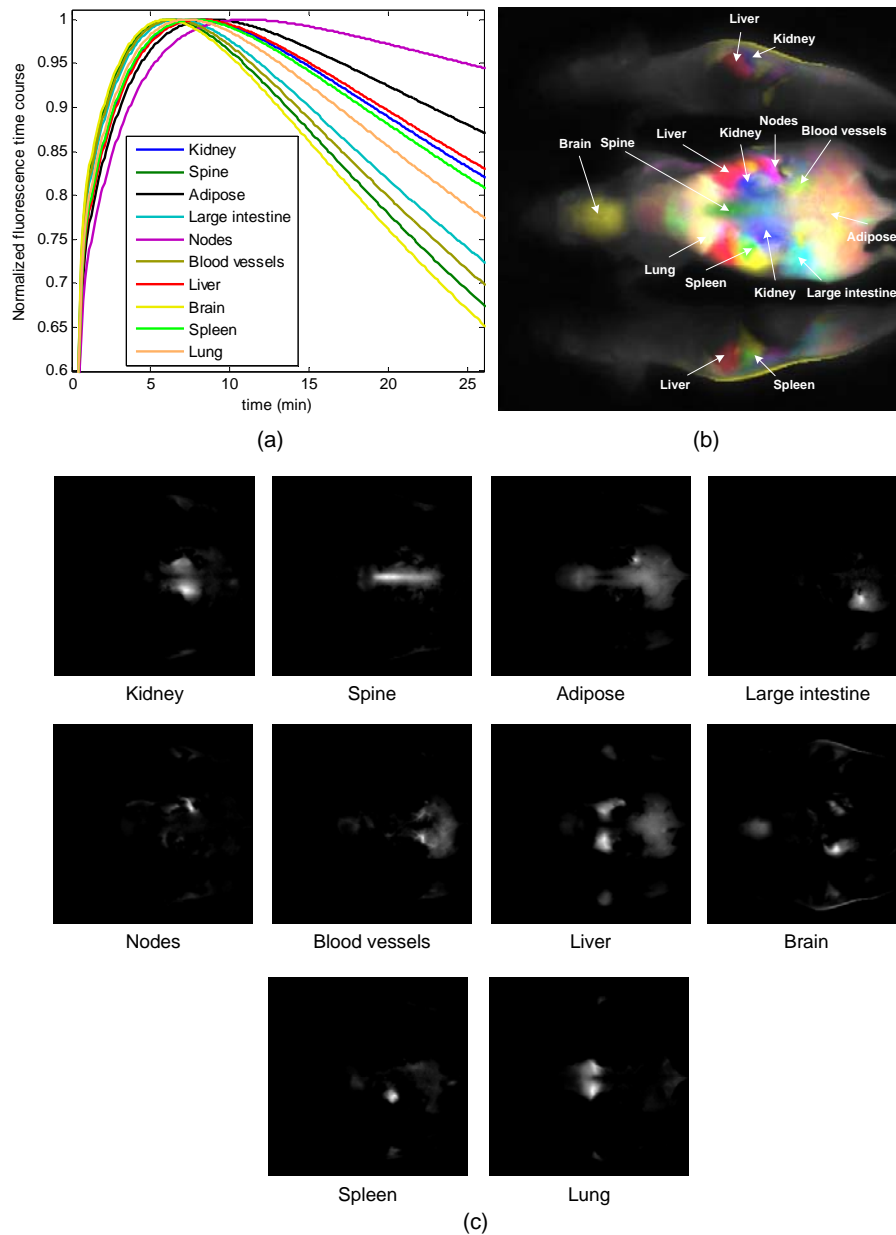|	Bladder	Adipose	Large intestine	Small intestine	Liver
K_j^{In}	0.9265	0.8187	0.7447	0.9665	1.0670
k_j^{Out}	0.0431	0.0482	0.0560	0.0263	0.0068

Figure S6. The results of CAM-CM on dynamic fluorescence images of a prone position small mouse. (a) Ten normalized fluorescence time courses estimated by CAM-CM. (b) Merged and color-coded spatial maps of the major organs. (c) Individual spatial maps of the ten major organs.
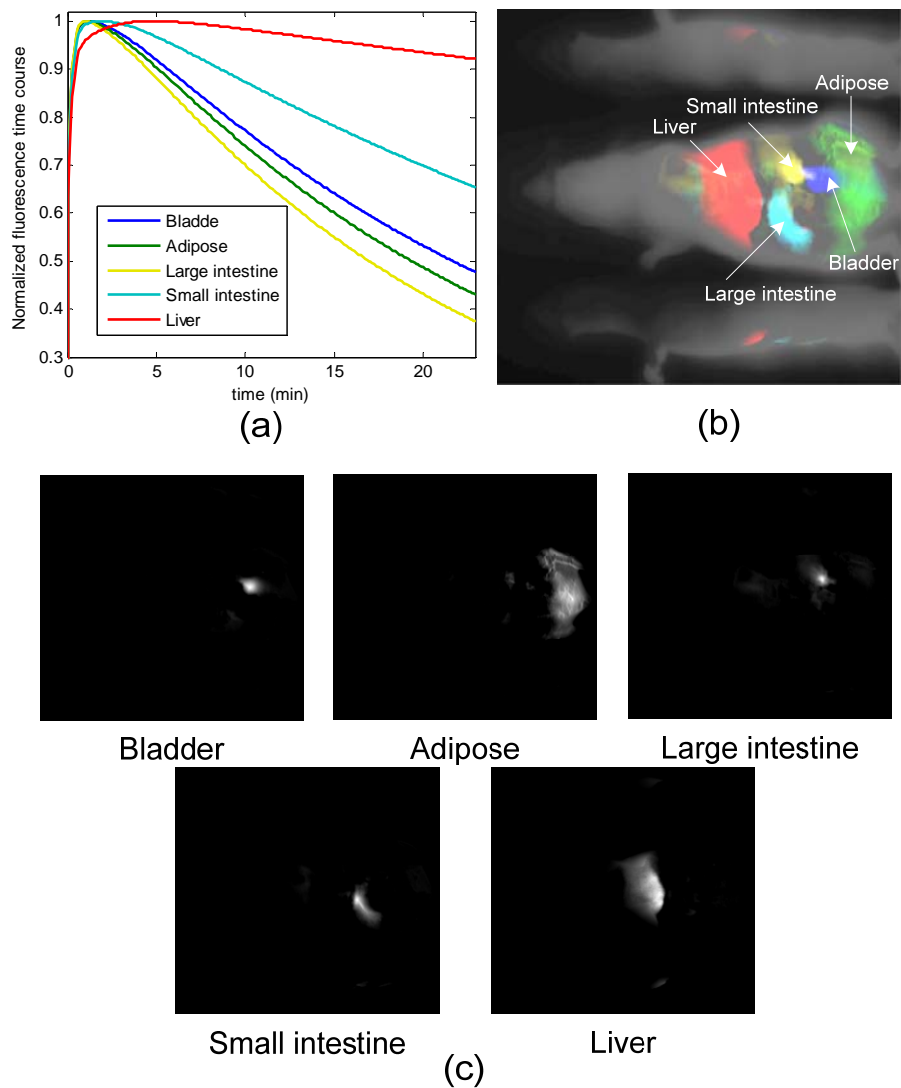
Figure S7. The results of CAM-CM on dynamic fluorescence images of a supine position small mouse. (a) Five normalized fluorescence time courses estimated by CAM-CM. (b) Merged and color-coded spatial maps of the major organs. (c) Individual spatial maps of the five major organs.

S5.3 A longitudinal case study on DCE-MRI data

As an example of more complex problems, we considered the datasets arising from a longitudinal study of tumor response to anti-angiogenic therapy using similar imaging protocols (**Figs. S8-S10**) (Choyke*, et al.*, 2003; Costouros*, et al.*, 2002; McDonald*, et al.*, 2003). Three sets of DCE-MRI data were acquired before, during, and after the treatment period, each three months apart, serving as the potential endpoints in assessing the response to therapy.

On dataset 1 (baseline), our CAM-CM analysis reveals two biologically interpretable compartments with distinct physiological kinetic patterns (**Fig. S8c**). They are associated with local wash-in constants maps with a significant fraction (72.4%) of partial volume pixels (**Fig. S8d**), which can be visually observed from the "filled" three-corner equal-lateral convex hull of the projected pixel time series scatter plot (**Fig. S8a**). This represents a relatively less aggressive and early stage breast tumor with relatively higher permeability $k_f^{Out} = 1.787\,\text{min}^{-1}$ in its fast-flow pool and relatively lower permeability $k_s^{Out} = 1.031\,\text{min}^{-1}$ in its slow-flow pool. As expected, local wash-in constants maps do not show any visible rim-shape region of aggressive angiogenesis or inner-core region of hypoxia but rather more uniform distributions of the two compartments.

On dataset 2 (the same tumor, acquired during the treatment), our CAM-CM analysis reveals two biologically interpretable compartments with distinct, yet with much closer physiological kinetic patterns (**Fig. S9c**). They are associated with local wash-in constants maps with a significant fraction (61.8%) of partial volume pixels (**Fig. S9d**), which can be visually observed from the "filled" three-corner convex hull of the projected pixel time series scatter plot (**Fig. S9a**). The CAM-CM estimated local wash-in constant maps reveal disconnected and reduced regions of localized angiogenesis and connected and enlarged regions of normalized tissue (**Fig. S9d**).

On the dataset 3 of the same tumor acquired after the treatment period, our CAM-CM analysis reveals two similar compartments with largely converged physiological kinetic patterns (**Fig. S10c**). They are associated with local wash-in constants maps with a significant fraction (59.4%) of partial volume pixels (**Fig. S10d**), which can be visually observed from the blended obtuse-isosceles triangle convex hull of the projected pixel time series scatter plot (**Fig. S10a**). The CAM-CM estimated local wash-in constant maps reveal globally reduced yet only isolated angiogenic activities (**Fig. S10d**).

The outcomes of CAM-CM analysis here are plausibly consistent with the reported observations on tumor response to antiangiogenic therapy (Choyke*, et al.*, 2003; Jain, 2005; McDonald*, et al.*, 2003; Padhani, 2003; Padhani*, et al.*, 2001; Turkbey*, et al.*, 2010; Yankeelov*, et al.*, 2007). The interaction between angiogenic inhibitors and tumor vasculature is a complex process depending upon the doses and timing of the applied therapeutic agents (Jain, 2005; Padhani*, et al.*, 2001). For example, controlled antiangiogenic therapies not only destroy aggressive angiogenesis but also transiently "normalize" the abnormal structure and function of surviving tumor vasculature to make it more efficient for oxygen and drug delivery. Initial results from trials of angiogenesis inhibitors monitored with DEC-MRI suggest that before therapy, the tumors are often highly and heterogeneously perfused and permeable, while soon after successful therapy begins, dramatically decreased perfusion and permeability can be detected (Choyke*, et al.*, 2003; McDonald*, et al.*, 2003). In breast cancer, a decrease in transendothelial

permeability has been reported to accompany tumor response to therapy (Choyke, *et al.*, 2003; Padhani, *et al.*, 2001). We note that tumor induced vascular activities were significantly reduced as an early response to therapy, where most noticeable is the large and consistent drop in the relative fraction of the $K_f^{In}(i)$ map and permeability rate k_f^{Out} (slower initial enhancement, decreased amplitude, slower wash-out) (Choyke, et al., 2003). We note that the tumor vasculature is intrinsically heterogeneous and, as a result, the whole tumor region may not demonstrate responses to antiangiogenic therapy that occur in some parts of the tumor but not in other parts (Turkbey, et al., 2010). We also note that tumor islands of persistent enhancement have escaped the effects of therapy, representing previously reported foci of resistant and more aggressive clones within a tumor (Choyke, et al., 2003; Padhani, 2003). Once again, the CAM-CM estimated values of $k^{Out} = 0.56 \sim 2.46$ min^{-1} were generally consistent with the parameter values of $k^{Out} = 0.88 \sim 1.93$ min^{-1} reported by the most relevant studies (Knopp, et al., 1999).
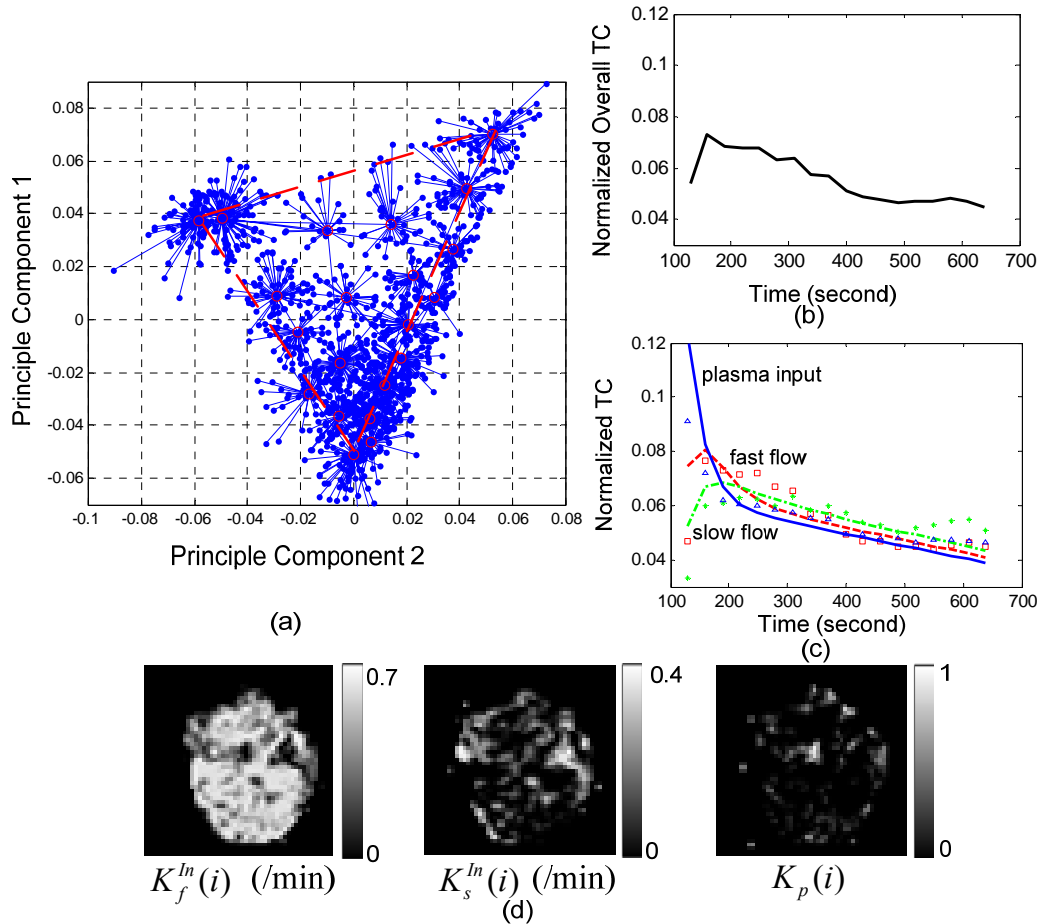

Figure S8. The result of CAM-CM on DCE-MRI dataset 1 of the breast cancer longitudinal study. (a) Identified convex hull of clustered pixel TCs (Blue dots: normalized pixel TCs; Red circles: cluster centers; Blue lines: cluster memberships). (b) Normalized overall TC calculated from the entire tumor ROI. (c) Normalized compartment TCs estimated by CAM-CM. (d) Local wash-in constant maps estimated by CAM-CM.
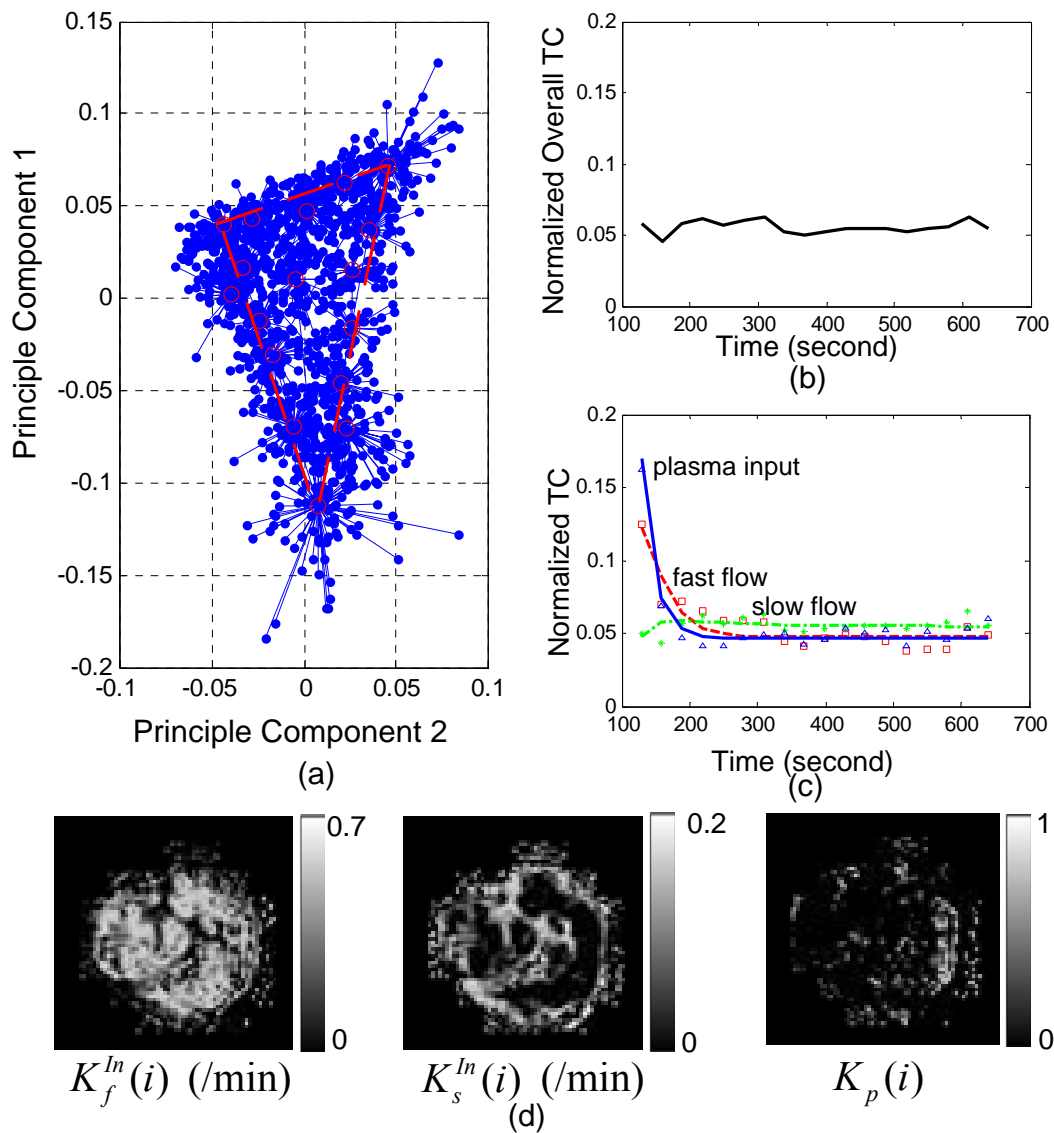
Figure S9. The result of CAM-CM on DCE-MRI dataset 2 of the breast cancer longitudinal study.

(a)

(b)

(c)

(d)

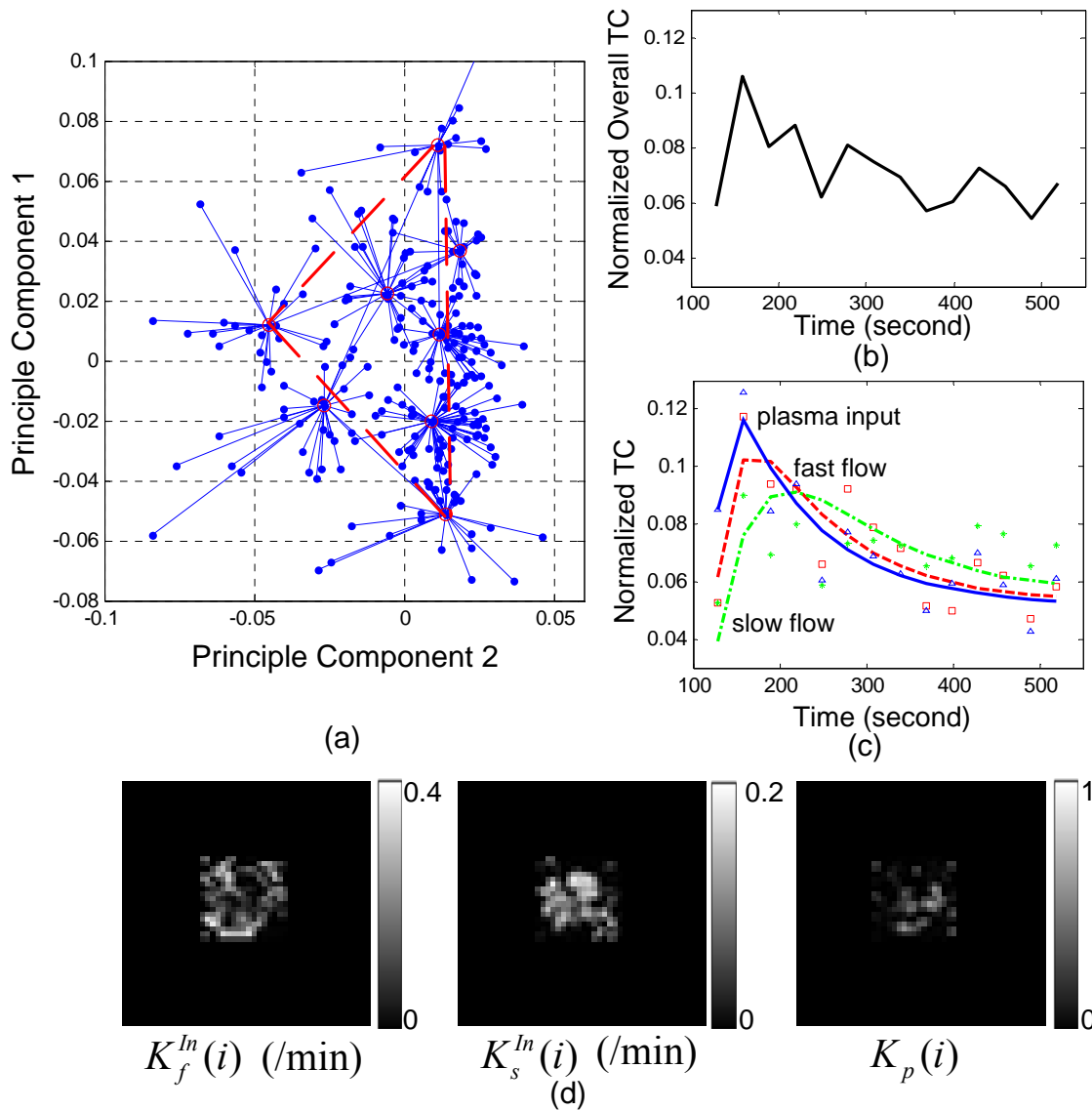$K_f^{In}(i)$ (/min) $K_s^{In}(i)$ (/min) $K_p(i)$

Figure S10. The result of CAM-CM on DCE-MRI dataset 3 of the breast cancer longitudinal study.

REFERENCES

Anderson, N.G., et al. (2010) Spectroscopic (multi-energy) CT distinguishes iodine and barium contrast material in MICE, *European Radiology*, **20**, 2126-2134.

Bishop, C.M. and Tipping, M.E. (1998) A hierarchical latent variable model for data visualization, *IEEE Transactions on Pattern Analysis and Machine Intelligence*, **20**, 281-293.

Boyd, S. and Vandenberghe, L. (2004) *Convex Optimization*. Cambridge University Press, Cambridge.

Brown, J.M. and Wilson, W.R. (2004) Exploiting tumour hypoxia in cancer treatment, *Nature Review Cancer*, **4**, 437-447.

Chen, L., et al. (2008) Convex analysis and separation of composite signals in DCE-MRI. *Biomedical Imaging: From Nano to Macro, 2008. ISBI 2008. 5th IEEE International Symposium on*. 1557-1560.

Chen, S., et al. (2004) Clustered components analysis for functional MRI, *IEEE Transactions on Medical Imaging*, **23**, 85-98.

Choyke, P.L., et al. (2003) Functional tumor imaging with dynamic contrast-enhanced magnetic resonance imaging, *J Magn Reson Imaging*, **17**, 509-520.

Costouros, N.G., et al. (2002) Microarray gene expression analysis of murine tumor heterogeneity defined by dynamic contrast-enhanced MRI, *Molecular Imaging*, **1**, 301-308.

Frey, B.J. and Dueck, D. (2007) Clustering by Passing Messages Between Data Points, *Science*, **315**, 972-976.

Hastie, T., et al. (2009) The elements of statistical learning: data mining, inference, and prediction. Springer, New York, NY, xxii, 745 p.

Haykin, S. (1999) Principal Component Analysis. In, *Neural Networks: A Comprehensive Foundation*. Prentice-Hall, New Jersey, 398.

Hillman, E.M., et al. (2007) Depth-resolved optical imaging and microscopy of vascular compartment dynamics during somatosensory stimulation, *NeuroImage*, **35**, 89-104.

Hillman, E.M.C. and Moore, A. (2007) All-optical anatomical co-registration for molecular imaging of small animals using dynamic contrast, *Nature Photonics*, **1**, 526-530.

Jain, R.K. (2005) Normalization of tumor vasculature: An emerging concept in antiangiogenic therapy, *Science*, **307**, 58-62.

Knopp, M.V., et al. (1999) Pathophysiologic basis of contrast enhancement in breast tumors, *J Magn Reson Imaging*, **10**, 260-266.

McDonald, D.M. and Choyke, P.L. (2003) Imaging of angiogenesis: from microscope to clinic, *Nature Medicine*, **9**, 713-725.

Miller, D.J. and Browning, J. (2003) A mixture model and EM-based algorithm for class discovery, robust classification, and outlier rejection in mixed labeled/unlabeled data sets, *IEEE Transactions on Pattern Analysis and Machine Intelligence*, **25**, 1468-1483.

Padhani, A.R. (2003) MRI for assessing antivascular cancer treatments, *The British Journal of Radiology*, **76**, S60-80.

Padhani, A.R. and Husband, J.E. (2001) Dynamic Contrast-enhanced MRI Studies in Oncology with an Emphasis on Quantification, Validation and Human Studies, *Clinical Radiology*, **56**, 607-620.

Port, R., et al. (1999) Multicompartment analysis of gadolinium chelate kinetics: blood-tissue exchange in mammary tumors as monitored by dynamic MR imaging., *Journal of Magnetic Resonance Imaging*, **10**, 233-241.

Rijpkema, M., et al. (2001) Method for quantitative mapping of dynamic MRI contrast agent uptake in human tumors, *Journal of Magnetic Resonance Imaging*, **14**, 457-463.

Roberts, C., et al. (2006) Comparative study into the robustness of compartmental modeling and model-free analysis in DCE-MRI studies, *Journal of Magnetic Resonance Imaging*, **23**, 554-563.

Segal, E., et al. (2007) Decoding global gene expression programs in liver cancer by noninvasive imaging, *Nature Biotechnology*, **25**, 675-680.

Titterington, D.M., et al. (1985) *Statistical Analysis of Finite Mixture Distributions*. John Wiley, New York.

Tofts, P.S., et al. (1999) Estimating kinetic parameters from dynamic contrast-enhanced T(1)-weighted MRI of a diffusable tracer: Standardized quantities and symbols, *Journal of Magnetic Resonance Imaging*, **10**, 223-232.

Turkbey, B., et al. (2010) The role of dynamic contrast-enhanced MRI in cancer diagnosis and treatment, *Diagnostic and Interventional Radiology*, **16**, 186-192.

Wang, F.Y., et al. (2010) Nonnegative least-correlated component analysis for separation of dependent sources by volume maximization, *IEEE Transactions on Pattern Analysis and Machine Intelligence*, **32**, 875-888.

Wang, Y., et al. (2006) Modeling and reconstruction of mixed functional and molecular patterns, *International Journal of Biomedical Imaging*, ID29707.

Yang, C., et al. (2007) Multiple reference tissue method for contrast agent arterial input function estimation, *Magnetic Resonance in Medicine*, **58**, 1266-1275.

Yankeelov, T.E., et al. (2007) Integration of quantitative DCE-MRI and ADC mapping to monitor treatment response in human breast cancer: initial results, *Magnetic Resonance Imaging*, **25**, 1-13.

Zhou, Y., et al. (1997) A modelling-based factor extraction for determining spatial heterogeneity of Ga-68 EDTA kinetics in brain tumors, *IEEE Transactions on Nuclear Science.*, **44**, 2522-2527.